Published on 21 December 2022. Downloaded by Korea Advanced Institute of Science & Technology / KAIST on 1/17/2023 2:13:38 AM.

Journal of Materials Chemistry C

ROYAL SOCIETY OF CHEMISTRY

PAPER

View Article Online
View Journal

Cite this: DOI: 10.1039/d2tc03751c

High-performance oxide thin-film diode and its conduction mechanism based on ALD-assisted interface engineering†

Hye-In Yeom,[a] Jingyu Kim,[a] Guk-Jin Jeon,[a] Jeongwoo Park,[b] Dong Uk Han,[a] Joohyeong Kim,[a] Kyung Min Kim,[a] Bonggeun Shong[b] and Sang-Hee Ko Park*[a]

Rectifying diodes have emerged as one of the promising components for advanced functional devices, including resistive random access memory and backplanes of active-matrix systems. Among various types of diodes, oxide thin film diodes have been extensively studied for their outstanding stability and rectifying characteristics. In this study, we developed a metal–oxide semiconductor–insulator–metal (MSIM) diode by atomic layer deposition-assisted interface engineering and obtained a high on–off ratio of $\sim 10^8$, low off-current density of 10^{-9} A cm^{-2} and good reliability. For the first time, the operation mechanism of the MSIM diode was also scrutinized with chemical analyses. X-Ray photoelectron spectroscopy and density functional theory results indicate that trimethylaluminum induced oxygen vacancies at the interface between InO_x and Al_2O_3 through a reduction reaction during Al_2O_3 deposition. The induced oxygen vacancies promote the formation of abundant tail states near the interface, and the tail states contribute to the injection of electrons from the cathode into Al_2O_3. From chemical and electrical analyses, suitable conduction mechanism and energy band diagram of the MSIM diode were proposed in detail. Consequently, the MSIM diode has been successfully demonstrated on a flexible polyimide substrate without degradation of rectifying characteristics, providing the potential of the MSIM diode as an advanced electronic device.

Received 6th September 2022,
Accepted 18th December 2022

DOI: 10.1039/d2tc03751c

rsc.li/materials-c

Introduction

Normally, inorganic oxide materials with wide energy band gaps such as Al_2O_3 and SiO_2 are essential components in diverse electric devices for their insulating properties. However, the electron can pass through the insulator by quantum tunneling or their internal defect states as the thickness is reduced. From the phenomenon described above, many studies have suggested the metal–insulator–metal (MIM) diode and tunneling diode, which can be used in random access memory.[1–3] The rectifying characteristics of these diodes, however, may not be controlled if the proper adjustment of defects and thickness uniformity in the insulator are not guaranteed. Therefore, it is necessary to develop another approach to fabricate thin-film diodes using the insulator.

Recently, diodes formed with an oxide semiconductor on an insulator (metal–insulator–oxide semiconductor, MIOS) have shown excellent rectifying characteristics.[4–6] The oxide semiconductor has uniform and stable electrical properties through s-orbital overlap based on metal–oxygen bonding.[7] Using the oxide semiconductor, which can induce stable charge injection and adjust the junction between the insulator and the semiconductor, it is possible to control the rectifying characteristics effectively. The first MIOS-based rectifying device was reported by Kim *et al.*[8] They initially deposited a solution-processed ZnO layer on a thermal oxidation-treated Si substrate and revealed that the ZnO layer acts as a buffer, injecting electrons from the cathode to the insulator. Unlike the conventional MIM diode, whose operation mechanism is governed by injection-limited conduction, the MIOS diode, where the current can even flow through thick insulators, exhibits an extremely low reverse current and high on–off ratio ($\sim 10^8$). Kim *et al.* further investigated the vertical current in an MIOS structure using other materials and approaches through defect engineering.[9–11] However, their device had limited practical applications because of the following reasons: (i) using a heavily doped Si substrate limits the usefulness of diodes in advanced applications, (ii) shadow-mask

[a] *Department of Materials Science and Engineering, Korea Advanced Institute of Science and Technology (KAIST), 291 Daehak-ro, Yuseong-gu, Daejeon, 34141, Republic of Korea. E-mail: shkp@kaist.ac.kr*

[b] *Department of Chemical Engineering, Hongik University, 94 Wausan-ro, Mapo-gu, Seoul 04066, Republic of Korea*

† Electronic supplementary information (ESI) available. See DOI: **https://doi.org/10.1039/d2tc03751c**

Published on 21 December 2022. Downloaded by Korea Advanced Institute of Science & Technology / KAIST on 1/17/2023 2:13:38 AM.

patterning is more complex and expensive than photolithography, and (iii) using a highly defective insulator to induce bulk-limited conduction can cause unexpected leakage current when integrated with other devices. In addition, Choi *et al.* reported a diode with an extremely high on–off ratio of $\sim 10^9$ using an indium–gallium–zinc-oxide (IGZO) heterostructure and a silicon nitride film.[12] Unlike Kim *et al.*, they deposited the insulator on top of the semiconductor, and suggested that the conduction through the insulator is due to the interfacial layer between them. However, they provided neither an in-depth analysis of the role nor exact mechanism of the interfacial layer formation.

Herein, we fabricated a high-performance metal–oxide semiconductor–insulator–metal (MSIM) diode by using atomic layer deposition (ALD) with a full photolithography process. The fabricated device exhibited a high on–off ratio of $\sim 10^8$. An abnormal growth behavior was observed at the interface between the InO_x and Al_2O_3 films. We attributed this phenomenon to the reduction reaction that occurred during deposition of the Al_2O_3 film by ALD. The abnormal behavior at the interface was systematically investigated to reveal the exact operation mechanism of the MSIM diode by using electrical and chemical analyses, as well as density functional theory (DFT). In addition, to demonstrate the application of the MSIM diode, the MSIM diode was implemented on a flexible polyimide (PI) substrate, and showed excellent electrical properties without any degradation regardless of laser lift-off process and bending test.

Experimental section

Fabrication of ALD-assisted MSIM diodes

MSIM diodes were fabricated on an ITO-coated glass (AMG). First, a 150 nm-thick ITO-coated glass was patterned as a bottom electrode. Subsequently, InO_x, Al_2O_3, and Mo film were sequentially deposited and the three layers were patterned by one mask. All patterning processes were performed through photolithography and wet etching. InO_x and Al_2O_3 films were deposited by plasma-enhanced atomic layer deposition (PEALD) at 250 °C and 200 °C, respectively. $Et_2InN(SiMe_3)_2$ and $AlMe_3$ (TMA) were used as precursors of each InO_x and Al_2O_3 film, respectively. Mo film was deposited by DC sputtering at room temperature. The thicknesses of InO_x, Al_2O_3, and Mo film were in the ranges of 1.5–10, 10–30, and 80 nm, respectively. The actual device size, where the top and bottom electrodes overlapped, was fixed at 50 μm × 50 μm.

Fabrication of a flexible MSIM diode

The PI-coated glass was fabricated by coating PI liquid (VTEC) on the glass and vacuum heat treatment at 380 °C. Si_3N_4 (170 nm) and Al_2O_3 (30 nm) were deposited on the PI-coated glass as buffer layers by plasma-enhanced chemical vapor deposition and PEALD, respectively. Then, the ITO (150 nm) bottom electrode was deposited by RF-sputtering, and the MSIM diodes were fabricated as described previously. Finally, the devices were delaminated by laser lift-off process.

Electrical measurement

The electrical properties were measured using an Agilent 4284A precision LCR meter and B4156A semiconductor parameter analyzer with a four-point probe station. All of the electrical properties (except thermal properties) were recorded at room temperature and under dark conditions.

Characterization for film property

The optical properties (absorption and reflectance spectra) were obtained by conducting UV-visible spectroscopy analysis (UV-vis, Shimadzu). Transmission electron microscopy (TEM) and scanning TEM (STEM) analyses were performed using a Cs-corrected STEM device (JEOL; JEM-ARM 200F) at an accelerating voltage of 200 kV. The work function was characterized by UV-photoelectron spectroscopy (UPS, Thermo VG Scientific). The chemical bonding states of In 3d and Al 2p and the valence spectra were characterized by X-ray photoelectron spectroscopy (XPS, Thermo VG Scientific). Reflection electron energy loss spectroscopy (REELS) analysis was performed to measure the band gap of the Al_2O_3 film using *in situ* XPS (Axis-Supra, Kratos).

Density functional theory calculations

Density functional theory (DFT) calculations were performed with the Vienna *ab initio* simulation package (VASP) with PBE functional, projector augmented wave (PAW) method, D3(BJ) dispersion correction, and DFT+U correction ($U_{\text{eff}} = U - J = 4.0$ eV).[13–17] The k-point grid sampling using the (5 × 5 × 1) Monkhorst-Pack mesh was used for optimization. The kinetic energy cutoff was set to 500 eV to reach the ground state configuration when the net forces on all ions were below 0.02 eV Å^{-1}. An In_2O_3 (111) slab was constructed to contain 6 In layers whose bottom 4 layers were fixed at bulk atomic positions, together with a vacuum space of 27 Å to avoid unphysical interactions. In order to model the adsorption reaction, we evaluated the adsorption energy (E_{ad}), defined as:

$$\Delta E_{\text{ad}} = E_{\text{molead}} - (E_{\text{slab}} + E_{\text{TMA}})$$

where E_{molead}, E_{slab}, and E_{TMA} are the total electronic energies of the relaxed supercell of the slab with adsorbates, the clean In_2O_3 slab, and the gaseous TMA molecule, respectively.

Results and discussion

Oxide thin-film diode with different structures

The optical microscopic image (top-view) and schematic structure of the oxide thin-film diode are shown in Fig. 1a. The overlapped region between the two electrodes determines the size of the effective diode area, which was 2500 μm^2 in this study. Three different kinds of devices were fabricated on the basis of structure and deposition sequence for the functional layers: a normal structure (3 nm-thick InO_x/20 nm-thick Al_2O_3, InO_x-first-stacked), an inverted structure (20 nm-thick Al_2O_3/3 nm-thick InO_x, Al_2O_3-first-stacked), and an MIM structure (20 nm-thick Al_2O_3 only). Fig. 1b shows the current

This journal is © The Royal Society of Chemistry 2022

Published on 21 December 2022. Downloaded by Korea Advanced Institute of Science & Technology / KAIST on 1/17/2023 2:13:38 AM.

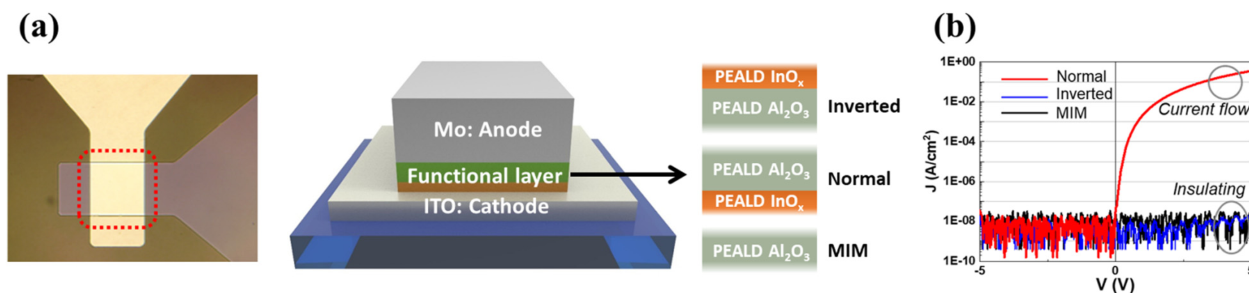

Fig. 1 (a) An optical image and schematic structure of the oxide thin-film diode. (b) Current density–voltage characteristics of the normal structure (red line), inverted structure (blue line) for the oxide-thin film diode, and MIM structure (black line).

density–voltage (J–V) characteristics of the devices. The normal structure device exhibits a low off-current density and excellent rectifying characteristics with an on–off ratio higher than 10^8, whereas the other devices show insulating properties in both voltage directions. The off-current density was measured at approximately $\sim 10^{-9}$ A cm^{-2} given the detection limit of the measurement system, indicating that the actual on–off ratio would be larger than 10^8. Although InO_x was in contact with the different electrode materials in each device, there was no major difference in the behavior of the electrons injected from the electrodes because the work function values of ITO (4.42 eV, from UPS analysis) and Mo (4.55 eV, from UPS analysis) are similar, and both the electrodes are in ohmic contact with the InO_x. Therefore, the only plausible reason for the variation in the electric behavior is the deposition sequence of InO_x and Al_2O_3, which strongly influences the physiochemical properties at the interface.

Interface characterization

Fig. 2a shows the UV-vis absorbance spectra of the 3 nm-thick InO_x, 20 nm-thick Al_2O_3, IA (InO_x-first-stacked), and AI (Al_2O_3-first-stacked) films. The reflectance effect can be excluded, as shown in the inset graph. The absorbance of both InO_x and Al_2O_3 films barely increases in the photon energy range of 1.5–3.5 eV, whereas the absorbance of the other stacked films increases. The absorption of light energy corresponds to the excitation of electrons. The band gap of the Al_2O_3 film analyzed by REELS is 7.6 eV, which is higher than 3.5 eV (Fig. S1, ESI†). In addition, the 3 nm-thick InO_x film does not have a sufficient number of electrons to be excited for a definite increase in the absorbance, although the relatively thick InO_x film has a band gap of approximately 3.5 eV.[18,19] Therefore, the enhanced visible light absorption of the stacked films is associated with the induced localized states at the interface and bulk Al_2O_3 during the deposition process.[20–22] Furthermore, between the two stacked films, the IA film exhibits a higher absorption in a wider range than the AI film. Based on these results, we conclude that more tail states are generated when Al_2O_3 is deposited on InO_x compared to the reverse deposition sequence, which explains the unusual rectifying behavior shown in Fig. 1b.

The cross-sectional TEM and annular dark-field–STEM images of the IA film on a Si wafer are shown in Fig. 2b. The images not only demonstrate the existence of the hetero-interfacial layer, but also reveal the occurrence of some deformation in up to nearly half of the Al_2O_3 film. Since the InO_x film is quite thin and vulnerable to high beam energies, it was difficult to ascertain the composition of the interfacial layer by energy dispersive spectroscopy. Therefore, the interfacial layer was analyzed using XPS, which is a powerful tool to infer the electrical properties of materials from their chemical bonding states.

XPS analyses of In 3d, Al 2p, O 1s, and valence chemical binding states along the IA film depth were performed using Ar sputtering for up to $\sim$620 s as part of the depth profile analysis (Fig. S2, ESI†). The spectra can be broadly categorized into three regions considering the spectral differences in the valence spectra: Al_2O_3 bulk region ($\sim$250 s), near interface region ($\sim$430 s), and interface-to-In bulk region ($\sim$620 s). Analyzing the O 1s peak is a more reliable method to confirm the oxygen binding state. However, it is difficult to separate O–Al and O–V_O because of their similar binding energies approximately at 531.5 eV.[23] Therefore, we scrutinized the other atoms and valence data to obtain the chemical information.

The XPS depth profiles of In 3d and Si 2p of IA film, and Si 2p of a single Al_2O_3 film are shown in Fig. S3 (ESI†). Si 2p was detected from the Si substrate. The In 3d peak of the IA film was primarily detected at a sputtered etch time of 250 s, whereas the Si 2p peak of the Al_2O_3 film was undetected even at a sputtering time of 300 s. The Si 2p peaks of the IA and Al_2O_3 films were first detected at 370 and 450 s, respectively. This brief comparison of the detection time of the atoms shows that indium atoms were diffused into the Al_2O_3 film, and formed a mixing layer during the deposition of the Al_2O_3 film.

Fig. 2c indicates that the Al 2p peak position is 74.68 eV until approaching the interface region, but moves slightly toward a lower energy by 0.25 eV in the interface-to-In bulk region. The peak shift is related to the change in the oxidation state or electronegativity of the nearby atoms.[24] This result suggests that a peak shift may occur because Al is less oxidized or other atoms with low electronegativity are mixed, such as indium instead of oxygen.

Deconvoluted In 3d spectra of the single InO_x film and the interface-to-In bulk region of the IA film are represented by Gaussian fitting from XPS narrow-scan (Fig. 2d). In the spectra, three chemical binding states were observed: In-OH (445.5 eV) species, fully oxidized In^{3+} (444.5 eV) species, and O-deficient In^{0-2+} (443.15 eV) species. A shoulder-like feature near 443.15 eV is observed in the InO_x/Al_2O_3 interface region, which

Published on 21 December 2022. Downloaded by Korea Advanced Institute of Science & Technology / KAIST on 1/17/2023 2:13:38 AM.

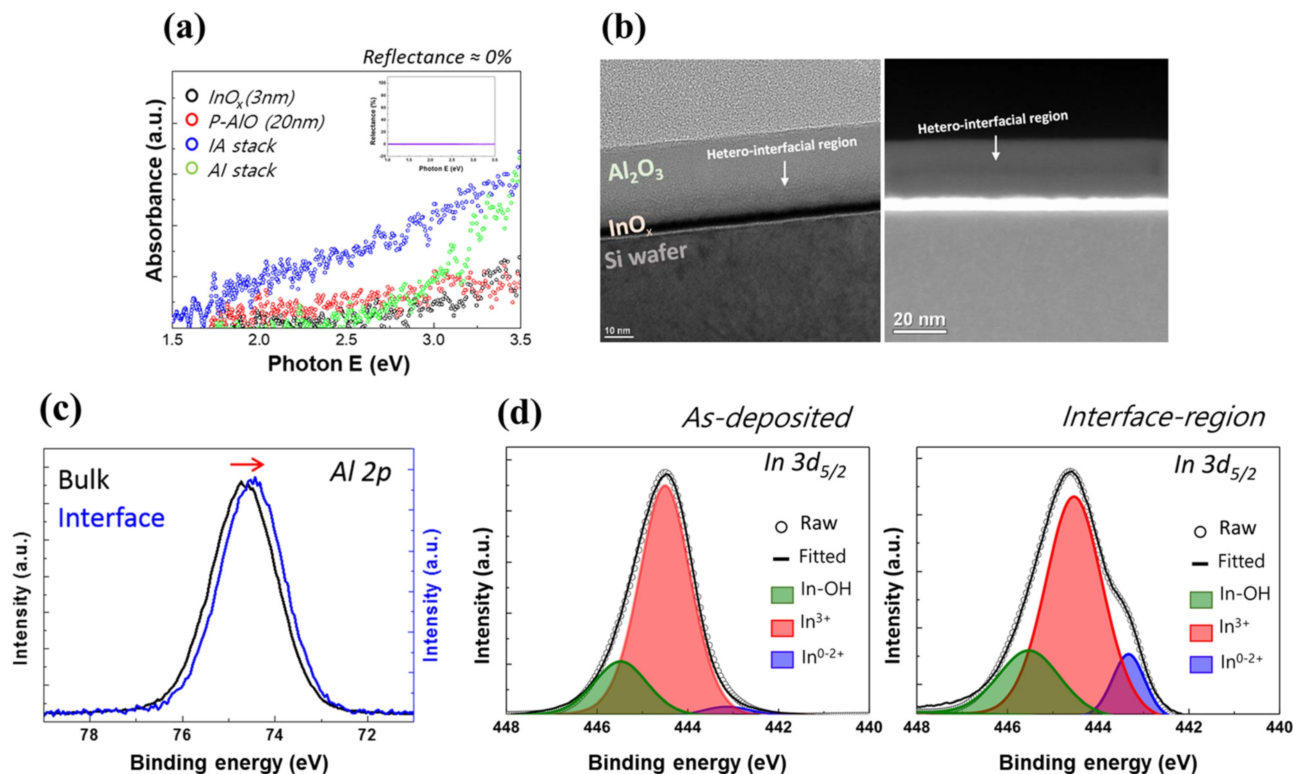

Fig. 2 (a) UV-visible spectroscopy with various film structures. (b) Cross-sectional TEM and STEM-ADF images of the IA stack film. (c) Al 2p peak of the IA stack film in X-ray photoelectron spectroscopy (XPS). The Al 2p peak is shifted to a lower binding energy that is closer to the InO_x/Al_2O_3 hetero-interface. (d) XPS analysis for the deconvoluted In $3d_{5/2}$ peaks of as-deposited InO_x film and interface region of the IA stack film.

means the oxidation state of the In 3d changed. The amount of In^{0-2+} increased from 3.94% to 11.41%, whereas the amount of fully oxidized In^{3+} decreased from 78.74% to 67.11%. These results indicate the generation of a highly reduced In species that would give rise to metallic property. We attribute the increase in reduced In species to the oxygen-extracting reaction during the ALD of Al_2O_3. The Al precursor used in this study, trimethylaluminum (TMA), possesses significantly high reactivity, so that it can either etch indium from the InO_x surface or extract the lattice (O_l) or interstitial oxygen (O_i) of InO_x, giving rise to an oxygen-deficient interface region.[25–27]

Fig. 3 demonstrates the DFT calculation results of TMA adsorption on the InO_x substrate during ALD to confirm that this reaction is energetically favorable. Given the facile reducibility of InO_x, the following mechanism is suggested for the surface reaction of TMA upon exposure to the InO_x surface. First, the surface of InO_x was assumed to have low density of OH groups at a temperature of 200 °C, at which the ALD of Al_2O_3 was experimentally performed.[28] Then, the TMA precursor would dissociatively adsorb, so that the released CH_3 ligands from TMA can react with the lattice oxygen of the substrate, releasing gaseous dimethylether as a byproduct.[29]

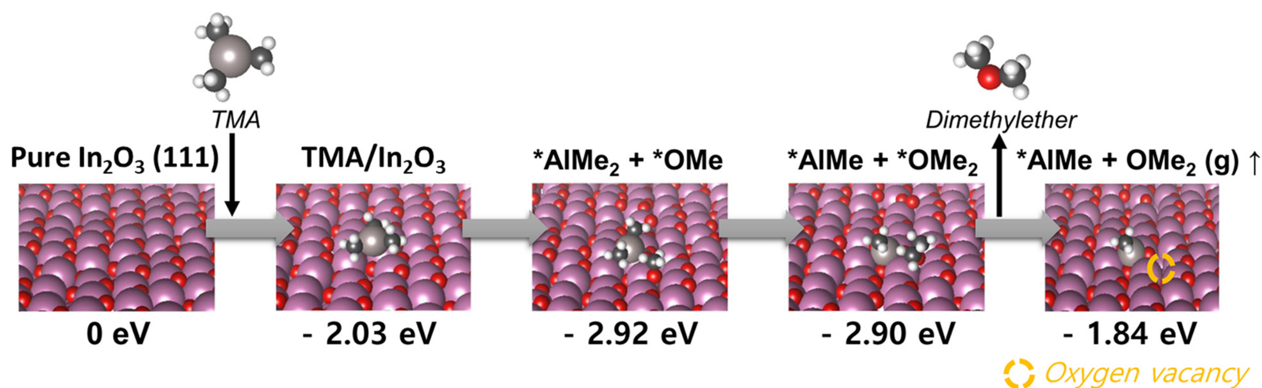

Fig. 3 Suggested TMA adsorption mechanism on the In_2O_3 (111) surface. Oxygen vacancy is formed by TMA and dimethylether (DME) is removed as a by-product (Purple: In, Red: O, Gray: Al, Black: C, White: H).

This journal is © The Royal Society of Chemistry 2022

Published on 21 December 2022. Downloaded by Korea Advanced Institute of Science & Technology / KAIST on 1/17/2023 2:13:38 AM.

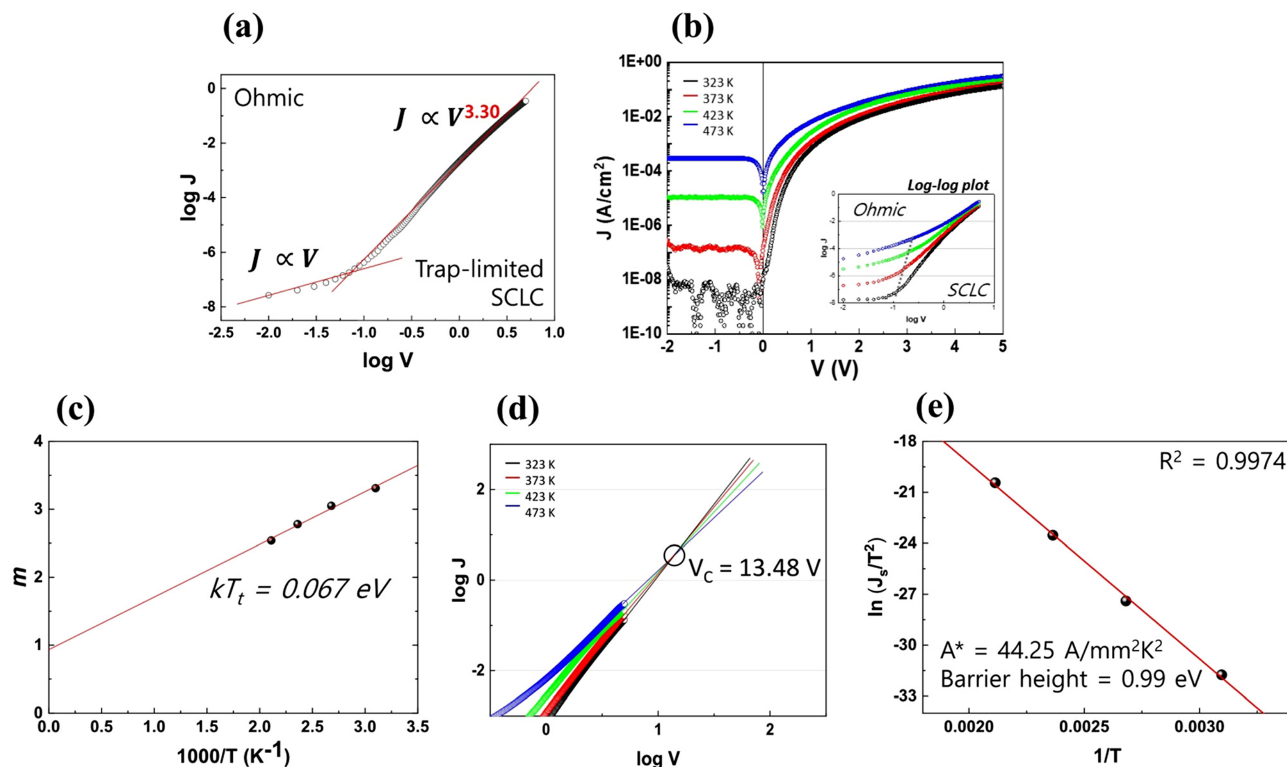

Fig. 4 (a) J–V relationship of the MSIM diode on a logarithmic scale. Fitted graph indicates that the trap-assisted space charge limited conduction is dominated in the vertical current flow in the device. (b) J–V characteristics of the MSIM diode under various temperatures (from 323 K to 473 K). The inset is the log–log scale at various temperatures. (c) Exponent value (m) *vs.* 1000/T graph of the MSIM diode. The value of kT_t (0.067 eV) was extracted from the slope of the fitted line. (d) log J–log V plot of the MSIM diode under various temperatures (from 323 K to 473 K), indicating that the critical voltage (V_c) is determined to be 13.48 V. (e) Richardson plot from the reverse saturation current density.

As a result, Al is irreversibly chemisorbed on the substrate, while the local oxygen vacancy is generated at the interface between Al_2O_3 and InO_x. Such reaction was assumed to occur in a step-by-step manner, as shown in Fig. 3. Overall, the surface reaction of TMA leading to formation of the interfacial oxygen vacancy can be considered facile, as the reaction energy is highly exothermic. The evolution of oxygen vacancies near the interface can also effectively decrease the diffusion barrier of indium atoms.[30,31] This result is analogous to the observation of indium diffusion in the near-interface mixing region. In addition, Klein *et al.* reported that the significant diffusion of oxygen from ITO destroys the self-limiting adsorption during the ALD of Al_2O_3.[32] They noted that the supply of oxygen from the ITO substrate prevents ALD-like growth during the first deposition of a few nanometers. Likewise, such an abnormal film growth can induce structural defects in the near-interface Al_2O_3 region. Overall, the ALD-assisted interface reaction can cause the evolution of oxygen vacancies that facilitates indium diffusion into bulk Al_2O_3, and also the defective growth of Al_2O_3. Therefore, it is necessary to reveal how this hetero-interface region influences the electrical properties of the diode.

Electrical analysis for MSIM diode

To verify the exact current flow mechanism through the insulator film, the current density data were fitted to various charge conduction mechanism model plots, including models based on Ohmic conduction, space charge limited conduction (SCLC), Schottky emission, Poole–Frenkel emission, and Fowler–Nordheim tunneling (Fig. S4, ESI†). Among them, the current density of the device linearly matched most closely with the SCLC model (Fig. 4a). As shown in Table S1 (ESI†), the relationship between the current density and the applied voltage follows $J \propto V^m$ when SCLC occurs. According to Child's law, the J–V relationship follows $J \propto V^2$ for trap-free SCLC, and trap-limited SCLC (TL-SCLC) occurs when m is higher than 2.[33,34] In the low-voltage region (<0.1 V), the current density is linearly fitted to the voltage (m = 1), implying that the Ohmic current flows through the insulator with its own high resistance. In the higher-voltage region (>0.1 V), the value of m is 3.30, which indicates that the TL-SCLC is the dominant conduction mechanism of the forward current flow in the MSIM diode. Since this conduction mechanism is bulk-limited, Ohmic injection occurs at the contact between the insulator and the semiconductor (or metal cathode). We assume that the interfacial reaction mentioned earlier might induce abundant states, resulting in the Ohmic injection. After the injection from the cathode, electrons would travel through the insulator by TL-SCLC.

Further electrical analysis was performed to interpret how the interface state is actually correlated with the electrical properties. The variation in the current with the temperature

Published on 21 December 2022. Downloaded by Korea Advanced Institute of Science & Technology / KAIST on 1/17/2023 2:13:38 AM.

provides information about the electrical conduction mechanism. Fig. 4b shows the *J*–*V* characteristics of the MSIM diode at various temperatures measured at voltages ranging from −2 to 5 V. In both voltage directions, the current density tends to increase with increasing temperature, whereas under a reverse bias ($V < 0$), the current density is independent of the voltage. In the region $V > 0$, the *J*–*V* curves are linearly fitted in a log–log plot for all temperatures, following $J \propto V^m$. The results indicate that the carrier conduction at all temperatures follows the bulk-limited conduction, as shown in Fig. 4b. The value of m gradually decreases with increasing temperature: 3.31 at 323 K, 3.05 at 373 K, 2.78 at 423 K, and 2.54 at 473 K. Assuming that the tail states are exponentially distributed in terms of the energy, we can express the *J*–*V* relationship by the formula:[35,36]

$$J = \left(\frac{qN_c\mu_O}{2}\right)\left(\frac{2\varepsilon_s\varepsilon_O}{qg_{tc}kT_t}\right)^l\left(\frac{V^{l+1}}{d^{2l+1}}\right)f(l) \quad (1)$$

where

$$f(l) = \left(\frac{1}{2}\right)^{l-1}\left(\frac{l}{l+1}\right)^l\left(\frac{2l+1}{l+1}\right)^{l+1} \quad (2)$$

$$g_{tail}(E) = g_{tc}\exp\left[\frac{E-E_c}{kT_t}\right] \quad (3)$$

The q is the electric charge, N_c is the effective density of the conduction band states, E is the electron energy, E_c is the conduction band energy level, and g_{tc} is the tail state density at E_c. The ε_s value for our actual device was 9.10, which was experimentally extracted from the capacitance–frequency curves (Fig. S5, ESI†). l is given by $l = m - 1 = kT_t/kT$. The exponent values of m are linearly fitted with T^{-1} under a forward bias, strongly implying that the electrons flow *via* a TL-SCLC with exponential tail states. kT_t, a characteristic energy parameter of the exponential tail states, was found to be 0.067 eV (Fig. 4c). Fig. 4d shows an enlarged log*J*–log *V* plot, where the dotted lines represent the experimental data points, and the solid lines are extrapolated from the dotted lines. As the electric field increases, the electrons start filling the exponentially distributed tail states, which are eventually filled at a certain critical voltage (V_c) that is independent of the temperature. The critical voltage is given by the function:[37]

$$V_c = \frac{qg_{tc}kT_td^2}{2\varepsilon_s\varepsilon_0} \quad (4)$$

The value of V_c can be obtained as 13.48 V from the intersection point of the extrapolated lines at all temperatures. Finally, we calculated the g_{tc} (3.80×10^{20} eV^{-1} cm^{-3}), using eqn (4). This value is much higher than those of other oxide semiconducting materials, such as a-IGZO (2×10^{19} eV^{-1} cm^{-3}) and a-ZTO (1.34×10^{19} eV^{-1} cm^{-3}).[38,39] The large number of tail states is attributed to the abnormal growth behavior during the sequential deposition of InO_x and Al_2O_3. The localized tail states near the hetero-interface region act as a limiting factor for the current compared to the trap-free materials.[35,36] Nevertheless, these tail states effectively reduce the conduction band minimum (CBM) and facilitate the injection of the electrons from the cathode into the Al_2O_3 layer.[40]

Since the current in the MSIM diode only increases with temperature in the region $V < 0$ regardless of the applied voltage, we attempted to fit the reverse saturation current value to meet the Schottky emission model. From the thermionic emission theory, we have the formula,

$$J_s = A^*T^2\exp\left[\frac{q\phi_{eff}}{kT}\right] \quad (5)$$

where ϕ_{eff} is the effective Schottky barrier height, and A^* is the Richardson's constant.[41] The reverse saturation currents at all temperatures were extracted from the average values in the flat region. With these values, the Richardson plot is obtained (Fig. 4e). The R^2 value is above 0.99, which implies that the thermionic emission model is reasonable to fully describe the increasing current phenomenon. A linear regression was performed on the data for temperatures ranging from 323 to 473 K to obtain the values of A^* (44.25 A cm^{-2} K^{-2}) and ϕ_{eff} (0.99 eV). The experimental barrier value of 0.99 eV was significantly lower than that calculated using the theoretical difference in the electron affinity between the Mo anode and Al_2O_3 (∼3.6 eV). We initially considered image force barrier reduction, which involves reducing the original barrier height by applying a negative bias to the metal electrode. However, the decrease in the barrier height is typically negligible ($\ll$1 eV). Therefore, the electrons from the Mo anode cannot be directly injected into the conduction band of Al_2O_3. In addition, the thermally excited electron–hole pairs cannot be the main reason for the current increase in negative voltage. This is because the increase in the reverse current is much greater than the increase in the forward current even with the same rise in temperature. Instead, we suspect formation of a current path in the Al_2O_3 film. The electron flow from the anode can explain the observation. A ''wake up effect'' was observed in our MSIM diode (Fig. S6, ESI†). In the first voltage sweep, the current suddenly increases at a certain forward bias. Subsequently, from the second sweep onward, the diode exhibits normal rectifying characteristics. This behavior represents a soft breakdown rather than a complete dielectric breakdown in terms of the current level and dielectric characteristics, indicating the formation of a permanent bidirectional current path in the Al_2O_3 film.[42] Notably, the current flow through the insulator does not necessarily imply that the dielectric property is deteriorated.[43,44] The evolution of the interface states can increase the likelihood of a local insulator degradation because of the increasing number of defects induced under a bias and the resulting current path. Because electrons move more slowly in Al_2O_3 than in InO_x, the electrons in the InO_x film are fully depleted under a reverse bias before the electrons arrive from Al_2O_3, leading to the formation of a potential barrier in the depletion region. This is why the MSIM diode shows an extremely low off-current. However, the electrons can overcome the potential barrier with the supplied thermal energy as the temperature increases, thereby leading to an increase in the off-current.

 This journal is © The Royal Society of Chemistry 2022

Published on 21 December 2022. Downloaded by Korea Advanced Institute of Science & Technology / KAIST on 1/17/2023 2:13:38 AM.

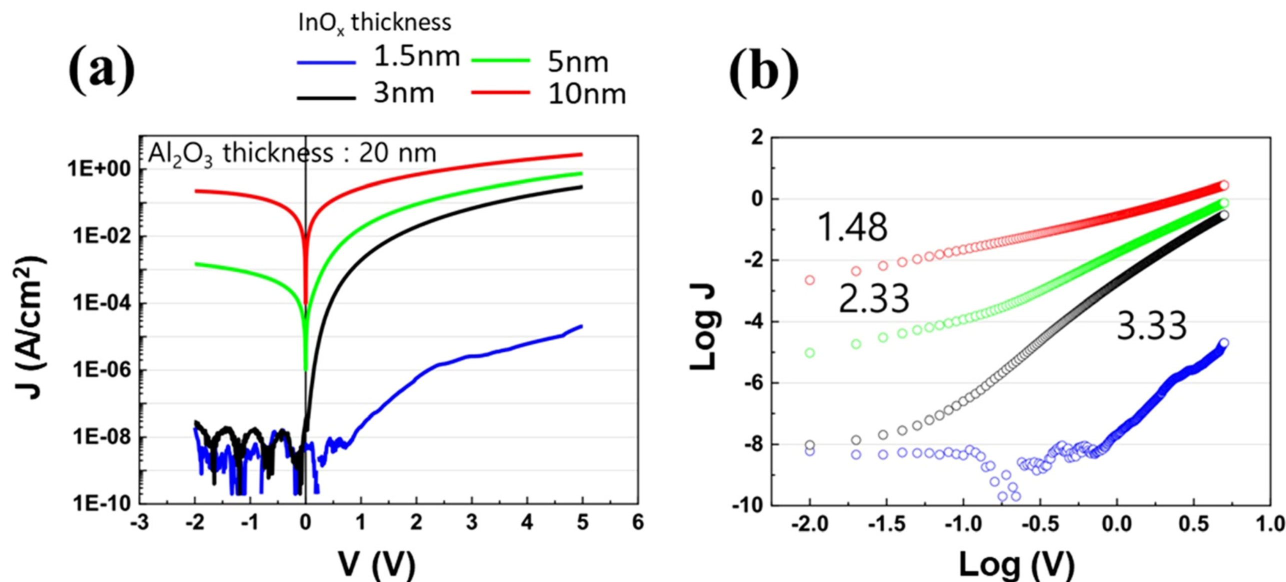

Fig. 5 (a) The J–V and (b) $\log J$–$\log V$ curves at InO_x thicknesses from 1.5 nm to 10 nm (Al_2O_3 = 20 nm).

To further investigate whether the depletion of InO_x actually affects the rectifying characteristics of the MSIM diode, Al_2O_3 using thermal ALD was applied to the MSIM diode. In the case of using Al_2O_3 deposited by thermal ALD instead of PEALD for MSIM structure, an Ohmic current was observed while thermal ALD Al_2O_3 itself showed excellent electrical insulation (Fig. S7, ESI†). This is due to the hydrogen incorporation to InO_x during the ALD because H_2O is used as a reactant in thermal ALD. Hydrogen is typically known as a shallow donor in oxide semiconductors, and can lead to the generation of free electrons.[45] They hinder the formation of an appropriate depletion region under reverse bias, resulting in non-rectifying bidirectional current conduction. Similar phenomena were observed when changing the film thickness of the InO_x film (Fig. 5a). Fig. 5b shows the $\log J$–$\log V$ characteristics with a thickness of InO_x film ranging from 1.5 to 10 nm. The thickness of the Al_2O_3 film was fixed at 20 nm. Under the forward bias, the on-current density increases with increasing thickness because of the increase in the number of electrons in the InO_x film. When the thickness is 1.5 nm, the on-current density at 5 V is quite low compared to that at other thickness values, less than 10^{-4} A cm^{-2}. Except for the 1.5 nm case, the exponent m values decrease with increasing thickness because the excessive carriers passivate the tail states. The off-current density mainly increased because of the limited formation of the depletion region. Eventually, the 10 nm-thick InO_x film exhibited Ohmic conduction (m = 1) in both bias directions, owing to the absence of a depletion region.

Possible band structure

The physiochemical properties of the MSIM diode were analyzed to reveal any correlation between them. From the findings, we suggest the possible band structures (Fig. 6a). The InO_x–Al_2O_3 layer can be broadly divided into two regions, namely (i) and (ii), in the depth direction, as noted in Fig. 6a. In region (i), the effective CBM appears to decrease near the interfacial region. This is because the induced V_O and In_i introduce shallow trap levels near the conduction band edge, acting as both electron donors and steps for the charge injection layer.[46] Based on the depth profile of the valence band maximum (VBM) spectra obtained from XPS (Fig. S3, ESI†), the VBM energy level decreases gradually from 3.88 eV (bulk Al_2O_3 region) to 2.56 eV (bulk InO_x region). Such continuous changes in both the VBM and CBM energy are correlated with the depth-resolved chemical composition change (inter-mixing layer). Notably, the reduction in the effective conduction band can facilitate electron injection. That is, the current flow mechanism can totally be governed by bulk-limited conduction instead of injection-limited conduction. In region (ii), intrinsic defects exist in the Al_2O_3 layer. Through the energy band diagram shown in Fig. 6b, we provide a plausible mechanism for the electron conduction in the MSIM diode. In the forward bias, electrons were injected from the metal cathode. Subsequently, TL-SCLC occurs as energetic electrons flow through the current path formed by inducing states between the intrinsic defect states in Al_2O_3. In the reverse bias, the electrons can move in the aforementioned current path formed after the "wake-up" effect. However, they cannot pass through the depletion region formed near the interfacial region and the InO_x layer. The inset shows the Mott–Schottky plot, indicating that the electrons are fully depleted at a bias lower than 0.24 V.

Demonstration on a flexible PI substrate

With the optimized characteristics of the MSIM diode on a flat glass substrate, we fabricated the flexible MSIM diodes on a PI substrate by employing the same photolithography process (Fig. 7a). The delaminated flexible MSIM diode exhibited no

Published on 21 December 2022. Downloaded by Korea Advanced Institute of Science & Technology / KAIST on 1/17/2023 2:13:38 AM.

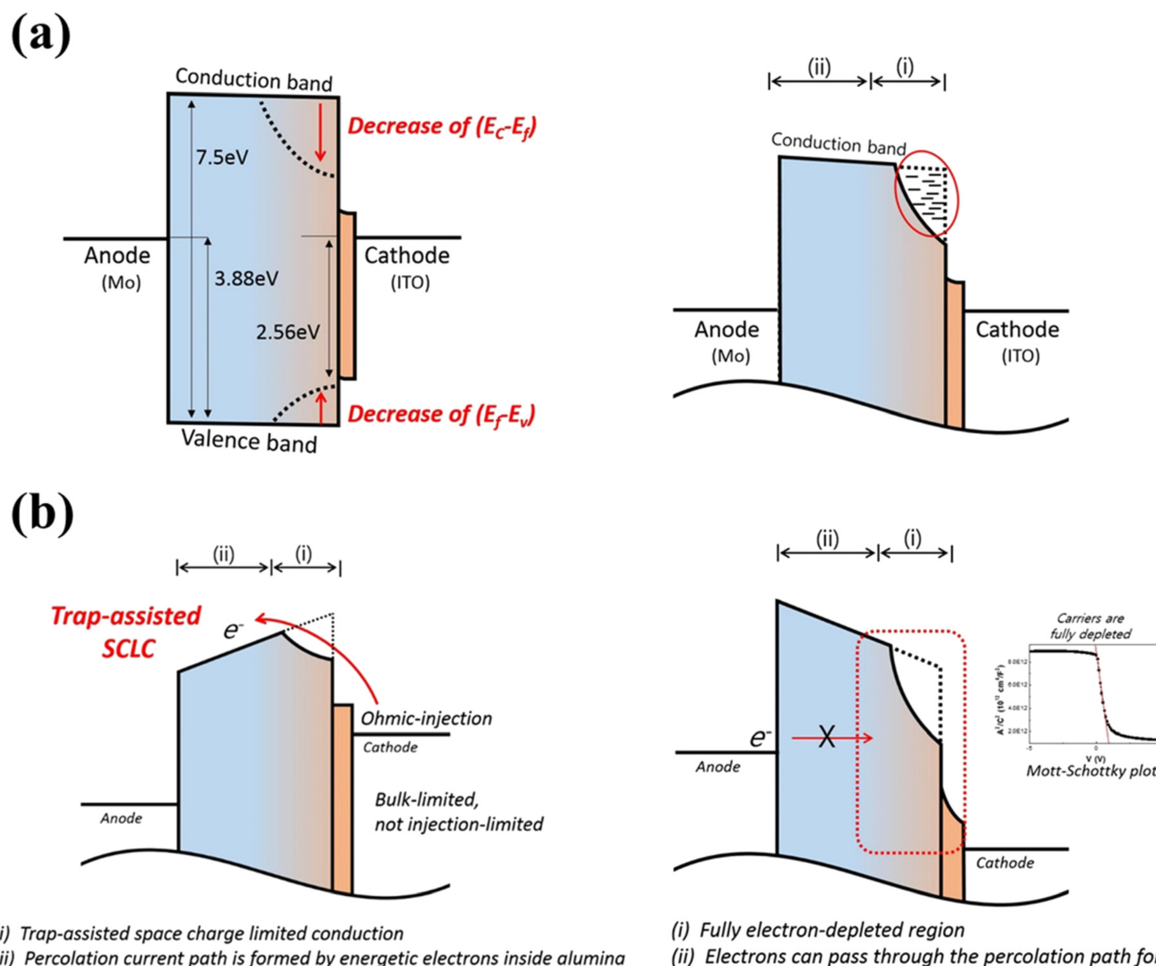

Fig. 6 (a) Schematic of the possible energy band diagram of the MSIM diode. (b) Possible mechanism for the electron conduction in the MSIM diode. When $V > 0$, current flows by trap-limited space-charge limited conduction; when $V < 0$, electrons cannot pass through the depletion region formed near the interfacial region and InO_x layer, resulting in no current flow.

electrical degradation after the laser lift-off process and the 1000 cycles of bending stress (bending radius: 5 mm), as shown in Fig. 7b. In addition, the 25 flexible MSIM diodes exhibited excellent electrical uniformity in terms of the on-current level of 0.24 ± 0.08 A cm^{-2} and on–off ratio of 7.24 ± 0.77 in log scale (Fig. 7c and d). Such reliable performance on a flexible substrate presents the applicability of the MSIM diode to the backplanes of advanced electronic devices.

Conclusion

In conclusion, we have developed a high-performance MSIM diode using ALD-assisted interface engineering. It showed high on–off ratio of $\sim 10^8$, low off current density of 10^{-9} A cm^{-2}, and outstanding uniformity. The sequential deposition of InO_x and Al_2O_3 was the key process to develop the rectifying diode. We attributed this phenomenon to a reduction reaction during Al_2O_3 deposition. The electron conduction in the MSIM diode was mainly governed by TL-SCLC, indicating that the properties of the film affected the current flowing through the insulator. Since TMA is a strong reducing agent, it could reduce InO_x by reacting with lattice oxygen and interstitial oxygen from InO_x, thereby leading to a huge generation of donor states near the interface. Therefore, we systematically investigated the abnormal behavior at the interface using electrical and chemical analyses, as well as DFT, to reveal the exact mechanism of the MSIM diode. The abnormal growth behavior at the interface between InO_x and Al_2O_3 was observed with the generation of oxygen vacancies formed by the reduction reaction in the InO_x layer. The evolution of oxygen vacancies facilitated the diffusion of the In atom, and generated numerous tail states near the interface. These tail states not only reduced the effective CBM, but also helped the electrons easily inject into Al_2O_3. Based on the findings, we proposed a film growth model and energy band structures in the MSIM diode. Finally, the MSIM diode was successfully demonstrated on a flexible PI substrate while maintaining electrical performance.

Conflicts of interest

There are no conflicts to declare.

 This journal is © The Royal Society of Chemistry 2022

Published on 21 December 2022. Downloaded by Korea Advanced Institute of Science & Technology / KAIST on 1/17/2023 2:13:38 AM.

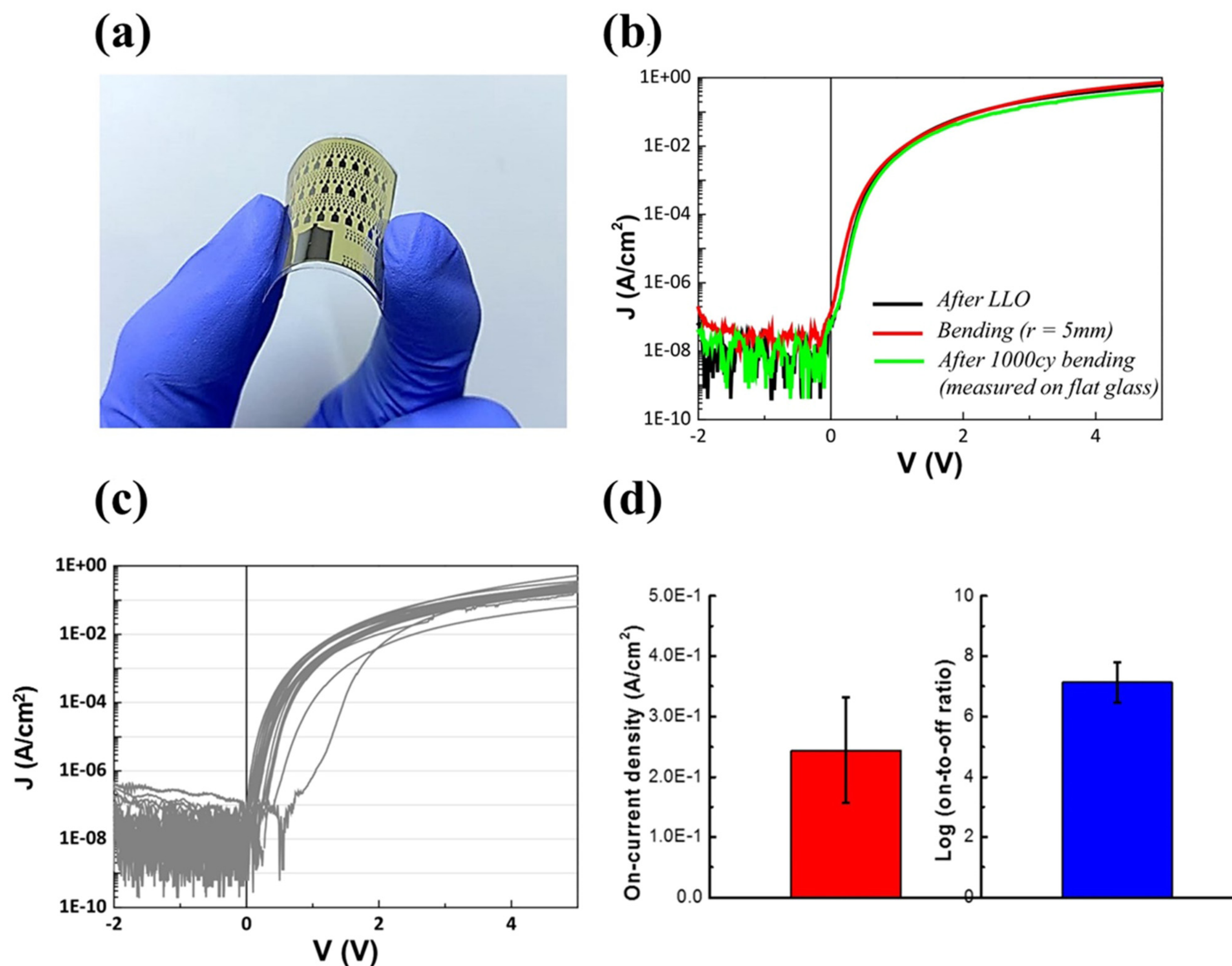

Fig. 7 (a) Photographic image of the flexible MSIM diodes. (b) J–V characteristics of the MSIM diode after laser lift-off (black), bent with radius = 5 mm (red), and after 1000 cycle of bending (green). (c) The J–V characteristics of 25 MSIM diodes. (d) Average on-current density and on–off ratio of the MSIM diodes.

Acknowledgements

This work was supported by the Industry Technology R & D Program (20006400) funded By the Ministry of Trade, Industry & Energy (MOTIE, Korea). This work was also supported by the Technology Development Program (S3207541) funded by the Ministry of SMEs and Startups (MSS, Korea).

References

1 W. Jeon, Y. Kim, C. H. An, C. S. Hwang, P. Gonon and C. Vallée, *IEEE Trans. Electron Devices*, 2018, **65**, 660–666.
2 A. H. Alshehri, K. Mistry, V. H. Nguyen, K. H. Ibrahim, D. Muñoz-Rojas, M. Yavuz and K. P. Musselman, *Adv. Func. Mater.*, 2019, **29**, 1805533.
3 W. Jeon, *J. Mater. Res.*, 2020, **35**, 775–794.
4 J.-W. Park, D. Lee, N.-K. Cho, J. Lee and Y. S. Kim, *ACS Appl. Electron. Mater.*, 2019, **1**, 530–537.
5 K. Kim, J.-W. Park, D. Lee, Y. H. Cho and Y. S. Kim, *ACS Appl. Mater. Interfaces*, 2021, **13**, 878–886.
6 J.-W. Park, D. Lee, K. Kim, Y. H. Cho and Y. S. Kim, *ACS Appl. Electron. Mater.*, 2020, **2**, 3946–3952.
7 K. Nomura, H. Ohta, A. Takagi, T. Kamiya, M. Hirano and H. Hosono, *Nature*, 2004, **432**, 488–492.
8 E. Lee, J. Lee, J.-H. Kim, K.-H. Lim, J. S. Byun, J. Ko, Y. D. Kim, Y. Park and Y. S. Kim, *Nat. Commun.*, 2015, **6**, 1–6.
9 J. Lee, K. Yoon, K.-H. Lim, J.-W. Park, D. Lee, N.-K. Cho and Y. S. Kim, *Sci. Rep.*, 2018, **8**, 1–9.
10 N.-K. Cho, J. Park, D. Lee, J.-W. Park, W. H. Lee and Y. S. Kim, *ACS Appl. Electron. Mater.*, 2019, **1**, 1698–1704.
11 D. Lee, J.-W. Park, N.-K. Cho, J. Lee and Y. S. Kim, Verification of charge transfer in metal-insulator-oxide semiconductor diodes via defect engineering of insulator, *Sci. Rep.*, 2019, **9**, 1–9.
12 M.-J. Choi, M.-H. Kim and D.-K. Choi, *Appl. Phys. Lett.*, 2015, **107**, 053501.
13 G. Kresse and J. Furthmüller, *Phys. Rev. B: Condens. Matter Mater. Phys.*, 1996, **54**, 11169.
14 J. P. Perdew, K. Burke and M. Ernzerhof, *Phys. Rev. Lett.*, 1996, **77**, 3865.

Published on 21 December 2022. Downloaded by Korea Advanced Institute of Science & Technology / KAIST on 1/17/2023 2:13:38 AM.

15 P. E. Blöchl, *Phys. Rev. B: Condens. Matter Mater. Phys.*, 1994, **50**, 17953.
16 S. Grimme, S. Ehrlich and L. Goerigk, Effect of the damping function in dispersion corrected density functional theory, *J. Comput. Chem.*, 2011, **32**, 1456–1465.
17 S. Dudarev, G. Botton, S. Savrasov, C. Humphreys and A. Sutton, *Phys. Rev. B: Condens. Matter Mater. Phys.*, 1998, **57**, 1505.
18 A. Walsh, J. L. Da Silva and S.-H. Wei, *J. Phys.: Condens. Matter*, 2011, **23**, 334210.
19 H.-I. Yeom, J. B. Ko, G. Mun and S.-H. K. Park, *J. Mater. Chem. C*, 2016, **4**, 6873–6880.
20 C. Á. Duke, *Phys. Rev.*, 1967, **159**, 632.
21 H. Yaghoubi, Z. Li, Y. Chen, H. T. Ngo, V. R. Bhethanabotla, B. Joseph, S. Ma, R. Schlaf and A. Takshi, *ACS Catal.*, 2015, **5**, 327–335.
22 H. Peelaers, E. Kioupakis and C. G. Van de Walle, *Appl. Phys. Lett.*, 2012, **100**, 011914.
23 N. Koslowski, S. Sanctis, R. C. Hoffmann, M. Bruns and J. J. Schneider, Synthesis, *J. Mater. Chem. C*, 2019, **7**, 1048–1056.
24 G. Greczynski and L. Hultman, *Prog. Mater. Sci.*, 2020, **107**, 100591.
25 S. Lee, M. Kim, G. Mun, J. Ko, H.-I. Yeom, G.-H. Lee, B. Shong and S.-H. K. Park, *ACS Appl. Mater. Interfaces*, 2021, **13**, 40134–40144.
26 S. Y. Lee, J. Kim, A. Park, J. Park and H. Seo, *ACS Nano*, 2017, **11**, 6040–6047.
27 S. Klejna and S. D. Elliott, *J. Phys. Chem. C*, 2012, **116**, 643–654.
28 A. Posada-Borbón and H. Grönbeck, *Phys. Chem. Chem. Phys.*, 2019, **21**, 21698–21708.
29 J. Park, H. Eom, S. H. Kim, T. J. Seok, T. J. Park, S. W. Lee and B. Shong, *Mater. Today Adv.*, 2021, **12**, 100195.
30 Y. Hu, C. Wang, H. Dong, R. M. Wallace, K. Cho, W.-H. Wang and W. Wang, *ACS Appl. Mater. Interfaces*, 2016, **8**, 7595–7600.
31 L. Ye and T. Gougousi, *ACS Appl. Mater. Interfaces*, 2013, **5**, 8081–8087.
32 T. J. Bayer, A. Wachau, A. Fuchs, J. Deuermeier and A. Klein, *Chem. Mater.*, 2012, **24**, 4503–4510.
33 F.-C. Chiu, *Adv. Mater. Sci. Eng.*, 2014, **2014**, 1–18.
34 Z. Zhu, J. Zhang, Z. Zhou, H. Ning, W. Cai, J. Wei, S. Zhou, R. Yao, X. Lu and J. Peng, *ACS Appl. Mater. Interfaces*, 2019, **11**, 5193–5199.
35 A. Rose, *Phys. Rev.*, 1955, **97**, 1538.
36 M. A. Lampert, *Phys. Rev.*, 1956, **103**, 1648.
37 V. Kumar, S. Jain, A. Kapoor, J. Poortmans and R. Mertens, *J. Appl. Phys.*, 2003, **94**, 1283–1285.
38 S. Lee and A. Nathan, *Appl. Phys. Lett.*, 2012, **101**, 113502.
39 Y. Son and R. L. Peterson, *Semicond. Sci. Technol.*, 2017, **32**, 12LT02.
40 T.-H. Chiang and J. F. Wager, *IEEE Trans. Electron Devices*, 2017, **65**, 223–230.
41 S. M. Sze and K. K. Ng, *Physics and Properties of Semiconductors—A Review, in Physics of Semiconductor Devices*, John Wiley & Sons, Ltd, 2006, pp. 5–75.
42 M. A. Alam, B. E. Weir and P. J. Silverman, *IEEE Trans. Electron Devices*, 2002, **49**, 232–238.
43 J. Jackson, T. Robinson, O. Oralkan, D. Dumin and G. Brown, *J. Electrochem. Soc.*, 1998, **145**, 1033.
44 D. Bharti and S. P. Tiwari, 2015 IEEE 15th International Conference on Nanotechnology (IEEE-NANO), IEEE, 2015, pp. 1015-1018.
45 K. W. Park, G. Jeon, S. Lee, J. B. Ko and S. H. K. Park, *Phys. Status Solidi A*, 2019, **216**, 1800737.
46 T. Tomita, K. Yamashita, Y. Hayafuji and H. Adachi, *Appl. Phys. Lett.*, 2005, **87**, 051911.

This journal is © The Royal Society of Chemistry 2022